CHEMISTRY OF MATERIALS

pubs.acs.org/cm

Article

An All-Solid-State Battery with a Tailored Electrode−Electrolyte Interface Using Surface Chemistry and Interlayer-Based Approaches

Sathish Rajendran,[§] Aparna Pilli,[§] Olatomide Omolere, Jeffry Kelber,* and Leela Mohana Reddy Arava*

Cite This: *Chem. Mater.* 2021, 33, 3401−3412

Read Online

ACCESS | Metrics & More | Article Recommendations | Supporting Information

ABSTRACT: Major challenges in the development of solid-state batteries using garnet-type solid-state electrolytes (SSEs) include suppressing dendrite growth, improving moisture stability, and reducing interfacial resistance. Prior attempts to remove surface impurities of SSEs through dry polishing caused high interfacial resistance that proves this method to be unviable. Further, several efforts on depositing thin-film protective layers on SSEs without understanding surface chemistry failed to demonstrate improved electrochemical performance. Here, we report the simultaneous removal of the surface impurities and protection of the SSE against air and moisture by regulating its surface chemistry. In situ X-ray photoelectron spectroscopy (XPS) studies revealed that primary surface contaminants such as lithium carbonate (Li_2CO_3) and lithium hydroxide on the SSE, $Li_{6.5}La_3Zr_{1.5}Ta_{0.5}O_{12}$ (LLZT), could be removed by either argon-ion sputtering at 227 °C or annealing at 777 °C in ultrahigh vacuum conditions. To protect the cleaned LLZT surface from further ambient contamination, in situ atomic layer deposition was used to deposit ∼3 nm-thick h-BN using tris(dimethylamino)borane and ammonia precursors at 450 °C. Intermittent XPS analysis confirmed the absence of Li_2CO_3 formation and the stability of h-BN-coated LLZT pellets for over 2 months of exposure to atmospheric air and moisture. Electrochemical impedance spectroscopy studies revealed that an ultrathin layer of ∼3 nm h-BN drastically reduced the interfacial resistance from 1145 to 18 Ω cm^2 (∼65× reduction). Li plating/stripping studies revealed a constant polarization of 27 mV at a 0.5 mA cm^{-2} current density over prolonged cycling and a high critical current density of 0.9 mA cm^{-2}. An all-solid-state battery using a $LiFePO_4$ cathode exhibited a stable capacity of 130 mAh g^{-1} for over 100 cycles and a negligible capacity fade-off of 0.11 mAh g^{-1} per cycle at an average Coulombic efficiency of 98.4%.

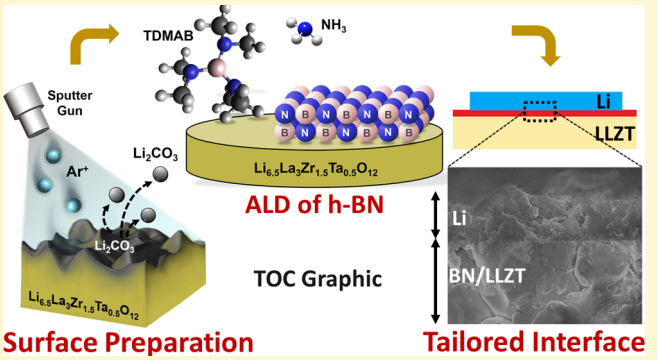

INTRODUCTION

The ever-burgeoning demand for portable electronic devices and electric vehicles has led to the need for high energy density lithium batteries. Lithium metal batteries (LMBs) that use a Li metal anode (the highest theoretical capacity of 3860 mAh g^{-1} and the lowest reduction potential of −3.04 V vs SHE) can essentially meet the energy demand of the future.[1−3] The use of metallic lithium in conventional LMBs, however, leads to severe chemical and mechanical instability issues due to their high reactivity with liquid organic electrolytes and propagation of Li dendrites.[4] An alternative approach is the use of solid-state electrolytes (SSEs) to replace organic liquid solvents that cause most of the safety issues in LMBs.[5,6] The all-solid-state battery (ASSB) technology holds great promise in large-scale energy storage devices. Among the different types of SSEs, candidates such as NASICON, sulfide-based glass electrolytes, and (Li, La)TiO_3 are not stable against metallic Li.[7] In contrast, a cubic garnet-type SSE has been found to possess high lithium-ion conductivity (10^{-3} S cm^{-1} at room temperature) and is macroscopically stable against metallic Li.[5] A garnet-type SSE also exhibits a wide electrochemical stability window (6 V vs Li/Li^+).[6,8] Although a garnet-type SSE has multiple advantages, a few grand challenges hinder its targeted applications. At the anode-SSE interface, microscopic investigation of the interaction between a cubic garnet-type SSE and metallic Li revealed transformation of several atomic layers of the cubic phase to the tetragonal phase.[9,10] Although mechanical stability at the cathode-SSE interface is an issue,[11] chemical interactions at the anode-SSE interface present major problems for further development. The lithium-rich SSE surface readily reacts with moisture and carbon dioxide present in the atmosphere to form lithium hydroxide (LiOH) and lithium carbonate (Li_2CO_3) on the surface.[12,13] In addition, the relatively high electronic conductivity of the garnet-type SSE induces tunneling of

Received: March 2, 2021
Revised: April 9, 2021
Published: April 26, 2021

electrons across the SSE, leading to lithium dendrite propagation.[14]

Several approaches have been proposed to overcome these challenges, including the use of (i) Li alloy anodes,[15,16] (ii) hybrid electrolytes,[17,18] (iii) 3-D structured anodes,[19,20] (iv) improved surface morphology,[8,21] and (v) interface modifications.[22−24] Among the various methods used, improving surface morphology and interface modification were found to be the most effective. For obtaining a high performing cell, the surface of the garnet-type SSE should be free from any impurities prior to the deposition of any buffer layer. Sharafi et al. introduced wet and dry polishing methods to remove Li_2CO_3 and LiOH on the surface of the garnet-type SSE to improve efficiency.[21] However, the critical current density was low to achieve a stable full-cell performance due to possibility of dendrite propagation across the interface, and such techniques are applicable only in smaller size SSEs due to the fact that thin SSEs are brittle. Thin-film barriers at the SSE surface, including Al_2O_3, ZnO, Si, and graphitic carbon, have been reported previously to modify the surface of the garnet-type SSE[22−24] but failed to focus on the surface chemistry of LLZT that determines the presence of surface defects and impurities, which subsequently induce dendrites limiting the cycle life performance at the full-cell level.[21] Hence, a combination of LLZT surface cleaning and interlayer-based modifications would benefit from the synergic effect of both the processes to achieve improved ASSBs. Although there are several reports on the interface improvement,[22,24−26] an in-depth understanding of the surface chemistry remains elusive.

Here, we demonstrate a surface chemistry-guided high-precision solution for simultaneous removal of impurities on the garnet-type SSE surface and protecting it against moisture, using ALD of hexagonal boron nitride (h-BN). This process involves first removal of Li_2CO_3 contamination on the surface of the SSE either by annealing of the garnet-type SSE at 777 °C in UHV or argon-ion sputtering at 227 °C followed by deposition of ultrathin films (∼3 nm) of h-BN by ALD. h-BN deposition using tris(dimethylamino)borane (TDMAB) and ammonia (NH_3) precursors forms a graduated BN_xO_y/BN capping barrier that protects the SSE surface against prolonged exposure to ambient, and it significantly improves cell performance. The noncorrosive TDMAB precursor was chosen rather than the conventional BCl_3 precursor to reduce the extent of corrosivity when combined with NH_3, which would in turn lower the oxidation of the LLZT surface. In this work, extensive surface chemistry studies were performed using in situ X-ray photoelectron spectroscopy (XPS), and the electrochemical properties of the improved interface were thoroughly investigated. Here, in situ XPS monitoring during the removal of surface impurities is highly essential to confirm their complete removal because transferring surface-cleaned LLZT from the chamber to the XPS instrument via an open atmosphere may result in the reformation of the surface impurities.

ALD is an attractive film deposition method for practical applications due to the fact that it is a self-limiting process that produces tailored conformal coatings, with atomic-layer control of film thickness.[27,28] Prior efforts utilizing ALD coatings for SSEs focused on Al_2O_3[24,29,30] and ZnO,[23] yielding some improvements in the wettability of SSEs with molten lithium. The cyclability of the full cell, however, remains a significant challenge. Two-dimensional (2-D) h-BN possesses unique electrical, optical, and mechanical properties.[31,32] The high chemical inertness of h-BN makes it stable against metallic Li, which is known for its high chemical reactivity.[25] Among the different methods of depositing h-BN, ALD has been reported to yield conformal, uniform coatings with superior mechanical properties.[31,33,34] As presented here, h-BN coating protects garnet-type SSEs from moisture-induced degradation. Galvanostatic cycling at 0.5 mA cm^{-2} for over 200 h further revealed that the h-BN layer effectively suppresses the propagation of lithium dendrites by preventing the tunneling of electrons across the SSE and also by creating a uniform lithium-ion flux that promotes homogeneous deposition of metallic Li. Further, fabrication of an all-solid-state battery demonstrates long, stable cycling performance for over 100 cycles using a $LiFePO_4$ (LFP) cathode.

EXPERIMENTAL SECTION

Synthesis of Solid-State Electrolytes. Garnet-type SSE with nominal composition of $Li_{6.5}La_3Zr_{1.5}Ta_{0.5}O_{12}$ (LLZT) was synthesized using conventional solid-state reaction.[35] Stoichiometric quantities of Li_2CO_3 (15 wt % excess), La_2O_3, ZrO_2, and Ta_2O_5, all purchased from Alfa Aesar with a purity of >99%, were taken as starting materials in a Teflon container, along with a small quantity of 2-propanol (Sigma-Aldrich, HPLC grade). This mixture was ball-milled for 8 h before vacuum drying at 80 °C. The obtained dry powder was calcined at 900 °C for 6 h at a heating rate of 2 °C min^{-1} using a muffle furnace (Thermolyne FB1315M). The resulting powder was again ball-milled for 20 h along with 2-propanol and then dried to get the LLZT powder. LLZT powder was then pressed into pellets using a uniaxial press (YLJ-15L, MTI Corp.). The pellets were covered with LLZT powder and sintered at 1160 °C for 16 h in air at a heating/cooling rate of 2 °C min^{-1}. The obtained pellets were later polished to a thickness of 250−300 μm in room atmosphere.

Surface Cleaning in an Ultrahigh Vacuum Chamber. The LLZT pellets were introduced into a multichambered vacuum system described elsewhere.[36] Briefly, the system consists of an atomic layer deposition (ALD) chamber and an ultrahigh vacuum (UHV) chamber at base pressures of 9×10^{-8} and 1×10^{-10} Torr, respectively. The UHV chamber was equipped with XPS and an ion sputter gun for sample cleaning. The chambers were isolated by manually operated gate valves, and sample transfer between chambers was accomplished using a magnetically coupled feedthrough without exposure to ambient. Resistive heaters in the UHV and ALD chambers permitted sample heating up to 927 °C. Temperatures were measured using a type K thermocouple mounted in proximity to the pellet. Vacuum in the UHV chamber was monitored using a nude ion gauge calibrated for N_2. Gas pressure in the ALD chamber was monitored using either a nude ion gauge or a Baratron capacitance manometer.

The surface contamination due to the formation of Li_2CO_3 on LLZT was removed either by UHV annealing or sputtering in an Ar^+ ion environment. The surface of LLZT pellets was cleaned by annealing to 777 °C in UHV in a series of steps, at a ramp rate of 1 °C/min. Sputtering was achieved by back filling the UHV chamber with 5×10^{-5} Torr of Ar gas at a beam voltage and emission current of 3 kV and 25 mA, respectively. The sample was maintained at moderate temperatures of 27−227 °C during the sputter process.

ALD of h-BN. The cleaned LLZT pellet was transferred from the UHV chamber to the ALD chamber, without exposing the sample to ambient. In situ ALD of h-BN was achieved by alternating exposures to TDMAB (Sigma-Aldrich, CAS# 4375-83-1, 99% purity) and electronic grade NH_3 (Praxair, CAS# 7664-41-7, >99.999% purity) at 450 °C. Although NH_3 gas was used without further purification, TDMAB was purified using a freeze−pump−thaw technique and distilled under vacuum into the chamber at room temperature due to its sufficiently high vapor pressure.[37]

ALD exposures are recorded in Langmuir (L; 1 L = 10^{-6} Torr s) and have not been corrected for ion gauge sensitivity or flux to the surface. The ALD process was optimized by monitoring the saturation

https://doi.org/10.1021/acs.chemmater.1c00747
Chem. Mater. 2021, 33, 3401−3412

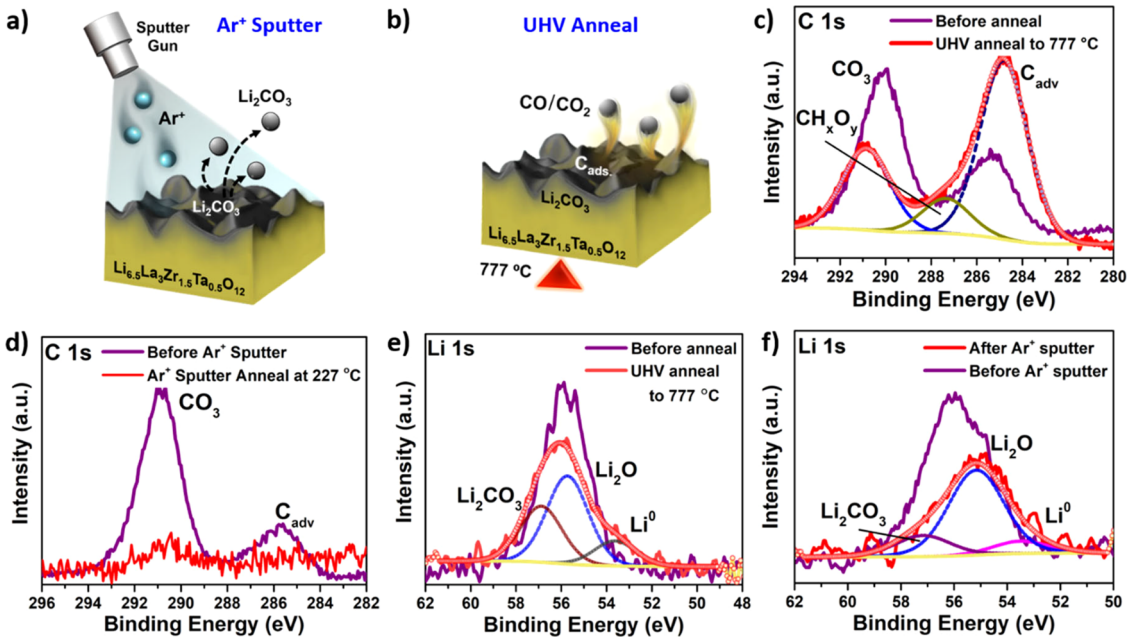

Figure 1. Schematic representation of LLZT surface cleaning using (a) Ar^+ sputtering and (b) UHV annealing at 777 °C. XPS of (c) C 1s after UHV annealing to 777 °C, (d) C 1s after sputter cleaning at 27−227 °C, (e) Li 1s after UHV annealing to 777 °C, and (f) Li 1s after sputter cleaning at 27−227 °C.

exposures of TDMAB and NH_3 on a clean LLZT pellet. The saturation dose for TDMAB was ~20.5×10^7 L, and for NH_3, it was ~90×10^7 L at 450 °C. The pellets were coated on both sides with h-BN, and the chamber was allowed to pump down to a base pressure of 1×10^{-5} Torr between ALD cycles.

Ambient Stability Measurements. After ALD, the h-BN-capped LLZT pellet (BN/LLZT) was exposed to air for 10 min, 30 min, 2 h, and 2 months at room atmosphere to examine its stability toward atmospheric moisture and carbon dioxide. Prior to h-BN deposition, the LLZT pellet was cleaned by annealing in UHV to 777 °C. LLZT annealed in UHV had significant elemental C and a negligible amount of Li_2CO_3 contamination prior to ambient exposures. After each exposure, the sample was transferred into the UHV chamber for XPS spectral acquisition.

Dendrites/Symmetrical Cells. Li|BN/LLZT|Li symmetrical cells were constructed by placing Li foil (approximately 15 mg cm^{-2}) on both sides of the BN/LLZT pellet and heating at 220 °C for 1 h after placing a load of 6 stainless spacers on the top side. Samples cleaned by Ar-ion sputtering to remove carbonate and other forms of contaminant surface C were then coated on both sides with h-BN by ALD (~3 nm on each side) and were used for the fabrication of the symmetrical cell. Custom-constructed Swagelok-type cells with a spring on one end to apply pressure were used for assembling the cell. The cells were double sealed with Teflon tape to prevent any leakage of air when removed from the glovebox. Galvanostatic plating/stripping of the lithium metal was done at constant current with time limitation.

Fabrication of the Full Cell. An all-solid-state battery with $LiFePO_4$|BN/LLZT|Li was constructed for galvanostatic cycling experiments. A lithium metal anode was attached to one side of the BN/LLZT pellet in the same way as described in the symmetrical cell assembly. The cathode composite consists of the active material, LLZT powder, super-P carbon, and a polyvinylidene difluoride (PVDF) binder in the ratio of 7:7:4:2. The active material ratio used here is in accordance with the literature.[38,39] Cathode composite components were converted to slurry in an *N*-methyl-2-pyrrolidone (NMP) solvent. The cathode composite slurry was spread over the solid electrolyte (attached with a Li anode) using an OHP sheet, which was then further placed on a hot plate inside the glovebox at 70 °C (the anode side facing down toward the heater) until the slurry was in a semidry state. Once the slurry is approximately 80% dry, the small amount of undried slurry on the top is scraped out using a clean glass slide. This also aids in obtaining a flat surface suitable for placing the stainless-steel current collector. Before placing the stainless-steel disc, the longer edge of the glass slide is used to create an impression on the semidry cathode such that the impression passes through the center of the solid-state electrolyte to prevent the trapping of evaporated NMP solvent in between the current collector and the cathode. After placing the stainless-steel disc, the setup was further dried in vacuum using the antechamber present in the glovebox at 90 °C for 12 h. The cathode composite loading was 8.8 mg cm^{-2} for the BN/LLZT long-cycling cell, 8.6 mg cm^{-2} for the BN/LLZT rate capability cell, and 8.1 mg cm^{-2} for the LLZT cell. The full-cell setup was transferred to a custom-made Swagelok cell that can apply a pressure of 126 kPa. Galvanostatic cycling was carried out from 2.8 to 4 V, while the cell was maintained at 60 °C in a hot air oven (MTI Corp.).

Material Characterization and Electrochemical Measurements. X-ray diffraction (XRD) analysis was performed using a D2 Phaser (Bruker), with a Cu Kα (1.5418 Å) radiation source in the range between 10 and 90° with a scan rate of 1° min^{-1}. Rietveld refining was performed using GSAS-II to obtain the crystal parameters. Field emission scanning electron microscopy (FE-SEM) images were obtained from a JSM 7600 JEOL instrument. A Biologic SP-150 potentiostat was used for the electrochemical impedance spectroscopy analysis in the frequency range of 7 MHz−1 mHz. An Arbin 36 channel cycler was used for the galvanostatic cycling experiments. The electrochemical cell preparation was carried out in an argon-filled glovebox (mbraun) that was maintained at O_2 < 0.5 ppm and H_2O < 0.1 ppm. XPS analysis was performed using a PHI Physical Electronics dual anode nonmonochromatic X-ray source, equipped with a hemispherical analyzer (VSW) with a mean radius of 100 mm and a multichanneltron detector (PSP Vacuum Technology). The spectra were acquired using Al Kα (1486.6 eV) radiation, operated at 300 W and 15 kV, and with the analyzer operating at a constant pass energy of 50 eV. All photoemission binding energies were calibrated to the La $3d_{5/2}$ feature at ~834.7 eV, instead of referencing to adventitious C.[40] The spectra were analyzed using commercially available software with capabilities for Shirley background subtraction, and the peaks were fitted using Gaussian−Lorentzian functions.[36] Average film thicknesses were calculated using inelastic mean free path (IMFP) lengths through the BN overlayer:

https://doi.org/10.1021/acs.chemmater.1c00747
Chem. Mater. 2021, 33, 3401−3412

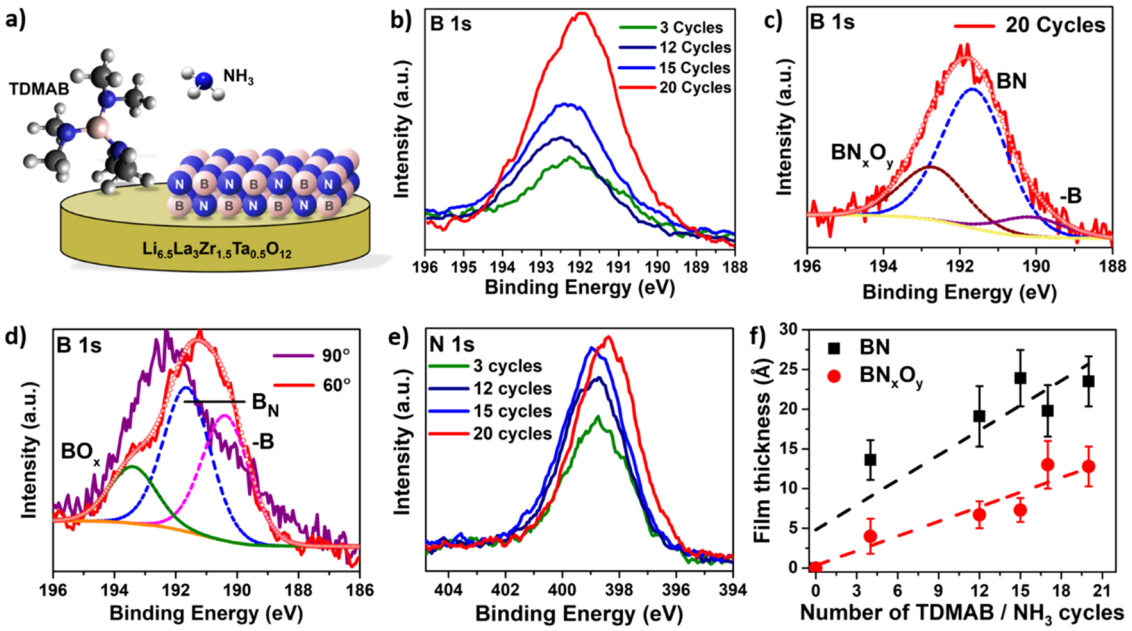

Figure 2. (a) Schemes of BN ALD using TDMAB and NH_3 precursors. Evolution of (b) B 1s XPS during ALD cycling, (c) deconvoluted B 1s after 20 TDMAB/NH_3 cycles on LLZT at 450 °C, (d) angle-resolved XPS of B 1s after 11 TDMAB/NH_3 cycles at 90° (purple trace) and 60° (red trace) emission angles, (e) N 1s XPS during ALD cycling, and (f) XPS-derived thicknesses of BN (black squares) and BN_xO_y (red circles) as a function of TDMAB/NH_3 cycles at 450 °C.

37.27, 30.05, and 34.42 Å for Li 1s, N 1s, and B 1s photoelectrons, respectively. The IMFP lengths were calculated using the TPP-2M IMFP predictive equation.[41] The relative atomic concentrations were estimated from the ratios of core-level XPS intensities as modified by atomic sensitivity factors but not corrected for IMFP. Most of the XPS spectra were acquired with the analyzer aligned with the sample normal ("normal emission"). Some spectra, however, were acquired at a shallow take-off angle with the analyzer aligned at 60° with respect to the sample normal ("shallow emission"), which decreases the effective IMFP and therefore the sampling depth, by ~50%,[36] thus increasing surface sensitivity.

RESULTS AND DISCUSSION

LLZT Synthesis and Characterization. The garnet-type SSE with nominal composition, $Li_{6.5}La_3Zr_{1.5}Ta_{0.5}O_{12}$ (LLZT), was synthesized by conventional solid-state synthesis, as described in our previous reports.[8,35] Ta-doped LLZT was selected because of its better cubic phase stability at room temperature and the higher lithium-ion conductivity compared to the undoped system. Rietveld refinement of XRD data of the synthesized LLZT powder was conducted, as shown in Figure S1a (Supporting Information). The profile fitting (R_{wp} of 7.92%) confirms the formation of a cubic phase with the space group *Ia*-3*d*, and the lattice parameter "*a*" was found to be 12.9107 Å, which is in alignment with the literature values, 12.9455[42] and 12.9101 Å.[43] The unit cell volume is calculated to be 2152.0556 $Å^3$. A cross-sectional FE-SEM (Supporting Information, Figure S1b) image shows dense morphology with very minimal voids and an average grain size of 13 μm. The relative density of the LLZT pellet was calculated to be 93% by taking the theoretical density of LLZT to be 5.4 g cm^{-3}.[44] Li-ion conductivity of synthesized LLZT was calculated through EIS measurements of LLZT attached with blocking electrodes on both sides of the pellet (Supporting Information, Figure S2). The conductivity values of 0.13 and 1.1 mS cm^{-1} were obtained at 22 and 60 °C, respectively, which match with the reported values.[45]

Surface Cleaning Process of LLZT. As-synthesized LLZT pellets displayed significant carbonate, adventitious carbon, and hydroxide contamination. This contamination not only shifted the XPS binding energies of core levels such as Li 1s, Ta 4f, O 1s, and C 1s regions but also masked the visibility of La and Zr precursors used in LLZT preparation (not shown). The pellets were either annealed in UHV to 777 °C or sputtered in an Ar^+ environment at 27−227 °C to remove contamination primarily in the form of Li_2CO_3. A schematic of the Ar^+ ion sputtering and UHV annealing is depicted in Figure 1a and Figure 1b, respectively, and the detailed analysis of garnet cleaning has been described elsewhere.[8] Figure 1c−f displays the evolution of C 1s and Li 1s XPS spectra after UHV annealing and sputter cleaning processes. UHV annealing to 777 °C (Figure 1c) shows a decrease in the C 1s intensity at 290.2 ± 0.4 eV corresponding to carbonate species[46] and a subsequent increase in intensity at ~285 eV. This broad, asymmetric carbon feature at lower binding energies can be resolved into two components corresponding to adventitious C at ~284.8 eV[47] and alkoxide (CH_xO_y) contamination at ~287.4 eV.[48] This decrease in C 1s intensity at higher binding energies and a subsequent increase at lower binding energies demonstrate that carbonate is being reduced to lower C oxidation states such as alkoxides ($C_xH_yO_z$) and hydrocarbons (C_xH_y) or adventitious C after the UHV annealing. Indeed, the melting point of Li_2CO_3 is ~727 °C, consistent with some decomposition of Li_2CO_3 after annealing to 777 °C.[49] The XPS-derived atomic concentrations of carbonate, adventitious C, and alkoxides were approximately 4.4, 13.5, and 2.4 at. %, respectively, after the final 777 °C annealing. In contrast, the C 1s XPS spectra obtained after 17 h of Ar^+ sputtering at 27−227 °C (Figure 1d) indicate complete removal of lower binding energy C, with a negligible amount of Li_2CO_3 species left on the surface at ~290.7 eV. These data demonstrate that pristine LLZT without significant surface C can be achieved by

https://doi.org/10.1021/acs.chemmater.1c00747
Chem. Mater. 2021, 33, 3401−3412

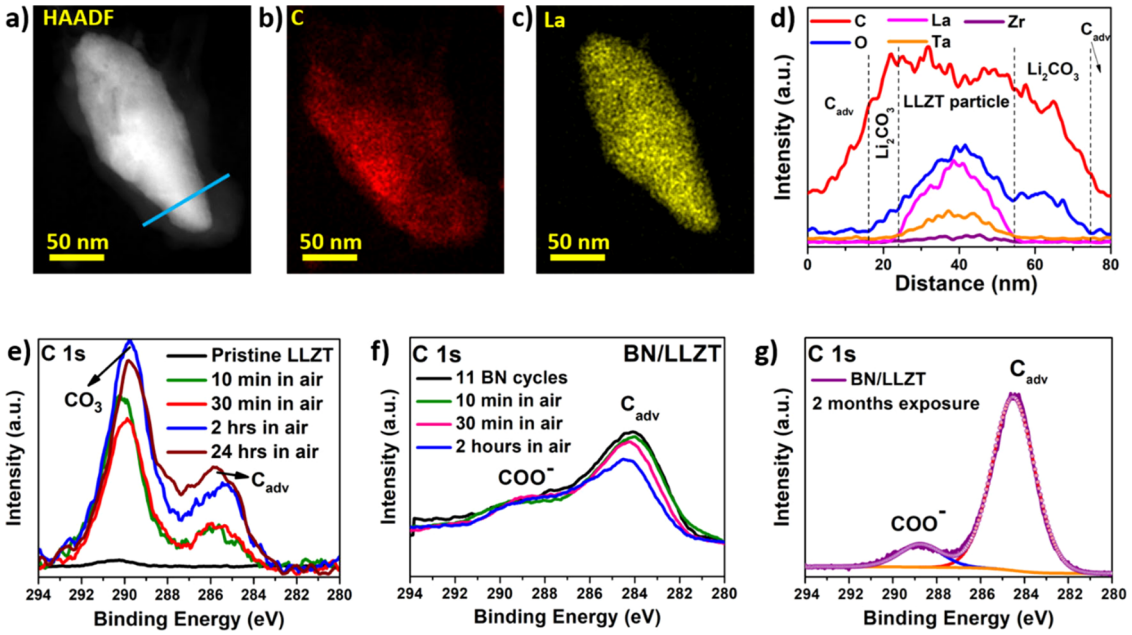

Figure 3. (a) HAADF-STEM imaging of as-synthesized LLZT. (b, c) Corresponding EDX elemental maps of C, and La. (d) EDX line map of the main elements along the line shown in (a). (e) Evolution of C 1s during ambient exposures of Ar^+ sputter-cleaned LLZT. (f) Evolution of C 1s during ambient exposures of h-BN-coated LLZT cleaned by UHV annealing for short exposure times. (g) XPS of C 1s after 2 months of ambient exposure of h-BN-coated LLZT cleaned by UHV annealing.

sputtering at mild temperatures, and the amount of Li_2CO_3 left on the surface was ~1 ± 1 at. %.

The mechanism for Li_2CO_3 removal by Ar^+ ion sputtering is clearly different from that of the UHV annealing method. Here, Li_2CO_3 does not convert into lower C oxidation states. Instead, the Li_2CO_3 layer is being etched off during sequential sputtering steps. The etching process starts with a complete removal of top surface contaminants like adventitious C and hydrocarbons at lower binding energies, within the first 2 h of sputtering. This is followed by almost complete removal of Li_2CO_3 even at low temperatures. The Li 1s spectrum in Figure 1e indicates a reduction in the Li 1s intensity and broadening toward lower binding energies after the UHV annealing. This reduction in intensity corresponds to some melting and decomposition of Li_2CO_3. The appearance of a new shoulder at lower binding energies of ~53.6 eV corresponds to a metallic Li (Li^0) feature.[50] The well-resolved Li 1s feature after the annealing can be decomposed into spectral components including residual Li_2CO_3, Li_2O, and Li^0 at 56.8, 55.8, and 53.6 eV, respectively.[50,51] However, the presence of some LiOH within the broad Li_2O peak at ~55.8 eV cannot be ruled out. The appearance of Li oxide and metallic Li denotes the reduction of Li_2CO_3 into lower Li oxidation states during the annealing process. The Li 1s spectrum after sputtering in Figure 1f also shows a decrease in intensity, similar to Figure 1e. Etching removed the Li_2CO_3 top layer revealing the underlying Li_2O and metallic Li features. Both sputtering and annealing techniques also revealed the XPS spectra of O 1s, Zr 3d, La 3d, and Ta 4f, which were initially obscured by a thick Li_2CO_3 top layer (not shown).

ALD of h-BN on LLZT. h-BN was deposited in situ on both sides of the LLZT pellets cleaned by either sputtering or annealing. Very similar results were achieved on both surfaces. Data are shown below (Figure 2) for deposition on a sputter-cleaned surface. ALD of h-BN was performed by alternating TDMAB and NH_3 exposures at 450 °C schematically shown in Figure 2a. Figure 2b–e displays the evolution of B 1s and N 1s XPS spectra during the ALD of BN. Figure 2b shows an increase in the B 1s intensity with an increasing number of TDMAB/NH_3 cycles, up to 20 cycles. The XPS spectra show a broad B 1s boron feature with an FWHM of ~2.5 ± 0.1 eV, suggesting the decomposition or reaction of some TDMAB precursor under the conditions employed, resulting in multiple B bonding environments. The B 1s feature in Figure 2b also shows a shift in the binding energy from 192 to 191.7 eV upon increasing the number of cycles between 3 and 20 cycles, respectively.

To better understand the various bonding environments of boron species, the B 1s acquired after 20 ALD cycles (Figure 2c) was decomposed into three components by constraining the full width at half maximum (FWHM) of all three components to be equal and ≤2 eV. The components at 192.7, 191.6, and 190.1 eV correspond to boron oxynitrides (BN_xO_y), boron nitride (B_N), and dangling boron bonds (−B), respectively.[52,53] The presence of boron oxynitride at a higher binding energy indicates the reaction of the TDMAB precursor with an oxygen-rich LLZT surface. A similar observation of the formation of boron oxide (B_2O_3) was reported during the deposition of BN on Li-Al-Ti-phosphate (LATP), using a chemical vapor deposition approach.[54] The data in Figure 2b,c suggest that boron oxide may have been converted into boron oxynitride due to oxygen–nitrogen exchange reactions, in the presence of excess NH_3 exposures. The presence of dangling boron bonds at ~190.1–189.5 eV also indicates the decomposition of TDMAB at elevated substrate temperatures. It should be noted that the intensity of the component at 191.6 eV is much greater than the combined intensities of BN_xO_y and dangling B components, demonstrating that most of the film growth is in the form of BN due to significant nitridation using the NH_3 precursor.

https://doi.org/10.1021/acs.chemmater.1c00747
Chem. Mater. 2021, 33, 3401–3412

B_2O_3 and BN_xO_y are unstable in air. Exposure of such films to ambient results in volatile boric acid formation.[55] Therefore, it is essential that the BN film is on top of the BN_xO_y layer, passivating both the oxynitride and the LLZT pellet. In order to determine the layer distribution, the take-off angle-resolved XPS spectrum was acquired after 11 TDMAB/NH_3 cycles at a shallow emission geometry, with the analyzer aligned at 60° from the surface normal. Figure 2d compares B 1s XPS acquired at normal and shallow emission geometries. At 60° emission, the B 1s spectrum consists of an intense BN peak at ∼191.6 eV and a small shoulder at ∼193.3 eV corresponding to BO_x bonds.[36] Since 60° emission is more surface-sensitive than normal emission, the data in Figure 2d confirms that BN forms the top layer with a BN_xO_y interface. The presence of such an interfacial layer along with dangling B atoms is indeed beneficial for Li-ion conductivity since the presence of such vacancies and defect sites aids in Li transport and improves the overall performance of the battery.[54] The corresponding N 1s XPS spectra in Figure 2e show an increase in intensity and a shift in binding energy from 398.8 to 398.4 eV after 20 TDMAB/NH_3 cycles at 450 °C. This slight shift in binding energy is consistent with initial BN_xO_y deposition and increasing BN formation with increasing ALD cycles. The N 1s peak can also be decomposed into two components at ∼398 and ∼399 eV, corresponding to BN and BN_xO_y, respectively.[56,57]

The evolution of XPS-derived average BN and BN_xO_y film thicknesses as a function of the number of TDMAB and NH_3 cycles is shown in Figure 2f. The corresponding B_N to N atomic ratios are displayed in Figure S3. Figure 2f shows a linear, ALD-type growth of BN and BN_xO_y layers with growth rates of ∼1 and ∼0.6 Å/cycle, respectively. These data demonstrate that thicker BN layers of ∼23.5 Å were deposited after 20 TDMAB/NH_3 cycles with a thin BN_xO_y interfacial layer of ∼12.8 Å thickness. The ratio of atomic concentrations of B_N to N, corrected by atomic sensitivity factors, is displayed in Figure S3 (Supporting Information). These data demonstrate the formation of stoichiometric h-BN films with a B_N to N ratio of 1.14 after 20 TDMAB/NH_3 cycles, on top of the BN_xO_y interfacial layer.

Surface Impurities around As-Synthesized LLZT. The as-synthesized LLZT powder was analyzed through high-angle annular dark-field scanning transmission electron microscopy (HAADF-STEM). The powder sample was stored in an argon-filled glovebox with O_2 < 1.2 ppm and H_2O < 0.1 ppm for 10 days prior to the HAADF-STEM characterization. As seen in Figure 3a, a thick amorphous layer of 2 to 10 nm could be observed surrounding the LLZT particle. This was further analyzed through energy-dispersive X-ray (EDX) analysis (Figure 3b,c and Supporting Information Figure S4), where the amorphous layer was found to be composed of carbon in most of the regions and some regions also showed the presence of oxygen atoms. Further, the EDX line profile was obtained over the line marked in Figure 3a and is shown in Figure 3d. The existence of La, Ta, and Zr along with carbon and oxygen can be attributed to the LLZT particle, and the immediate environment surrounding the particle consists of both C and O signals that correspond to the Li_2CO_3 and LiOH layer. Beyond this layer, there is only the C signal that corresponds to the adventitious carbon layer accumulated after the LLZT formation at 900 °C. These results prove the degradation of LLZT during synthesis and handling in ambient and the extent of reactivity of the garnet samples. Although these impurities surrounding the particle would be eliminated during sintering, this effect would be the same on the surface of the sintered pellet as the sintering is performed at ambient conditions. Hence, it is imperative to remove any such impurity layers formed on the LLZT pellet surface using methods as mentioned above, and the defect-free surface needs to be protected from further degradation when exposed to a moisture-containing atmosphere. Formation of impurities like Li_2CO_3 and LiOH around LLZT will have a detrimental effect during lithium-ion propagation, promoting the formation of lithium dendrites.[58]

Atmospheric Exposures of Pristine LLZT. The pristine garnet pellet was exposed to air for 10 min, 30 min, 2 h, and 24 h, after it was sputter-cleaned to remove all forms of surface C. Figure 3e and Figure S5a,b display the XPS of C 1s, Li 1s, and decomposed Li 1s spectra during sequential air exposures at room temperature. The C 1s XPS spectra in Figure 3e show a significant increase in intensity at ∼290.1 eV after 10 min of air exposure, and a smaller amount of reduced C buildup was observed at lower binding energies. The C 1s feature at ∼290.1 eV corresponds to Li_2CO_3,[22,59] and the feature at lower binding energies can be assigned to adventitious C at ∼285.5 eV[21,60] and alkoxide (CH_xO_y) at ∼287.3 eV.[48] Subsequent exposures to ambient resulted in a slight attenuation followed by a small increase in the Li_2CO_3 intensity at ∼290.1 eV after 30 min and 2 h in air, respectively. The Li_2CO_3 intensity attenuated further during 24 h of exposure. However, adventitious C and alkoxide features in Figure 3e and the O 1s XPS (not shown) indicated a gradual increase in intensity throughout air exposures. The total atomic percentage of Li_2CO_3 and lower binding energy C (adventitious C + CH_xO_y) was plotted as a function of air exposure times in Figure S6 (Supporting Information). Figure S6 demonstrates that ∼10.8 at. % Li_2CO_3 and ∼5.1 at. % lower binding energy C were formed within the first 10 min of LLZT exposure to air, and no significant change during subsequent air exposures was observed. The data demonstrate that Li_2CO_3 formation saturated in the first 2 h of LLZT exposure to ambient. Figure S5a (Supporting Information) displays the overlaid Li 1s spectra after 0 min (pristine LLZT), 10 min, 30 min, 2 h, and 24 h of air exposure. Li 1s shows an increase in intensity and a shift to higher binding energy after 10 min in ambient. There was a negligible change in Li between 10 and 30 min exposure times. Increasing exposure time to 2 h resulted in the appearance of a shoulder at a much higher binding energy (Figure S5a). However, Li 1s remains unchanged during the 24 h mark. To better understand the binding energy shifts in Li, the spectra were decomposed after 30 min and 2 h exposures in Figure S5b (Supporting Information). The deconvolution was performed by constraining the FWHM of all components to be equal to 1.5 eV. Figure S5b shows the presence of three components corresponding to Li_2O, LiOH, and Li_2CO_3 at ∼54.6, ∼55.8, and ∼57.2 eV, respectively.[59] However, after 2 h, the Li_2CO_3 shoulder at ∼57.2 eV increased significantly (Figure S5b, Supporting Information). The data in Figure S5a,b further demonstrate that all Li_2CO_3 were formed within the first 2 h of exposure, with no further increase in the shoulder feature at ∼57.2 eV during subsequent exposures to air. Since no significant change in the C 1s and Li 1s spectra was observed during the 24 h mark, it is safe to conclude that all Li_2CO_3 were formed within the first 2 h of LLZT exposure to air. These results also agree well with the proposed

https://doi.org/10.1021/acs.chemmater.1c00747
Chem. Mater. 2021, 33, 3401−3412

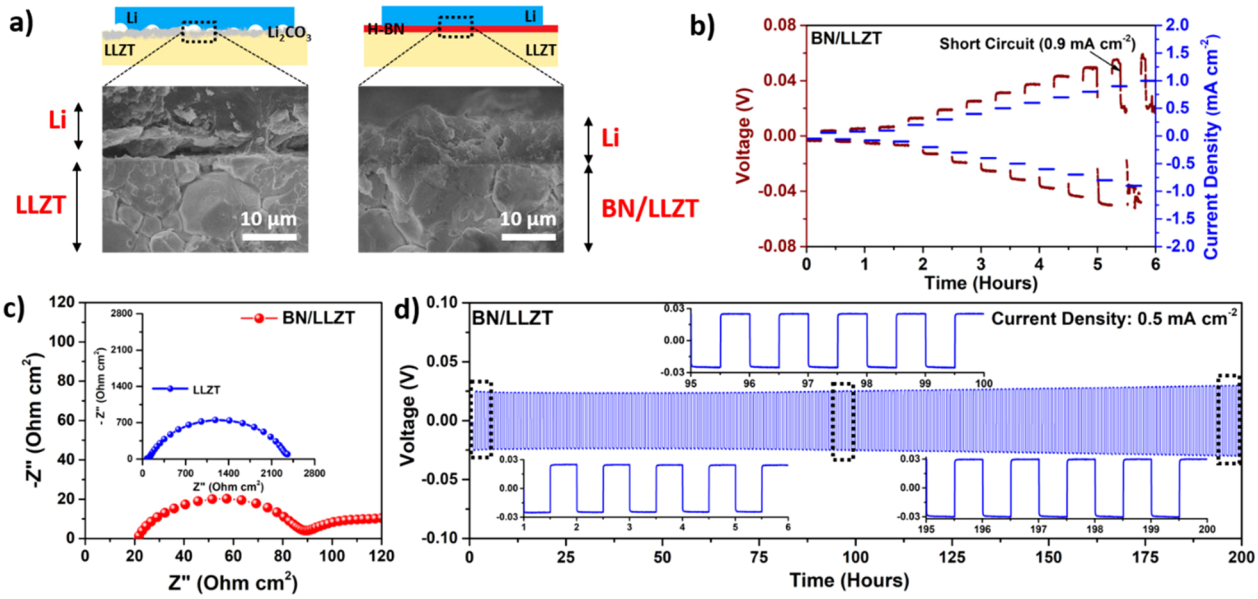

Figure 4. (a) Surface wetting property of metallic Li with as-synthesized LLZT and h-BN-coated surface-cleaned LLZT, (b) critical current density measurement using the BN/LLZT electrolyte, (c) EIS measurements of symmetrical cells, and (d) galvanostatic cycling of the symmetrical cell at a current density of 0.5 mA cm^{-2} and at 60 °C.

mechanism for Li_2CO_3 formation by Zhang et al., Cheng et al., and Truong and Thangadurai.[49,61,62]

Atmospheric Stability of h-BN-Coated LLZT. The chemical stability and structural integrity of h-BN-capped garnets (BN/LLZT) were examined by exposing the BN/LLZT pellet for 10 min, 30 min, 2 h, and 2 months to ambient. LLZT used for this experiment was initially annealed in UHV to 777 °C to remove Li_2CO_3 contamination. As ALD of h-BN on both annealed and sputter-cleaned Li garnet surfaces yielded similar results, the annealed sample was used for atmospheric stability measurements in order to determine if the reduced C layer present after annealing could affect in some way (e.g., pinholes) the passivating quality of BN. Annealing was followed by h-BN deposition along with a thin BN_xO_y interface formation after ALD cycles at 450 °C, similar to that observed for ALD on a sputter-cleaned surface. A combined film thickness of ∼3.1 nm was obtained after 11 TDMAB/NH_3 cycles with ∼24.2 and ∼7.1 Å of h-BN and BN_xO_y thicknesses, respectively. After the initial annealing treatment, the sample had some adventitious C contamination at ∼284.5 eV and a small amount of residual carbonate at ∼288.6 eV. The XPS spectra of C 1s, Li 1s, B 1s, and N 1s regions acquired during air exposures are displayed in Figure 3f,g and Figure S7 (Supporting Information). The C 1s spectra in Figure 3f show a gradual attenuation in the adventitious C feature at 284.5 eV after 10 min, 30 min, and 2 h of air exposure at room temperature. A small shoulder at ∼288.7 eV begins to appear after 10 and 30 min of air exposure, which further attenuates during the subsequent 2 h of exposure. This shoulder corresponds to carboxylate species (COO^-), which binds at a slightly lower binding energy than lithium carbonate (∼290.8 eV).[14] Such carboxylate contamination was also observed after ambient exposure of Al_2O_3-capped LLCZN.[14] Figure 3g displays the C 1s XPS spectrum after 2 months of air exposure. A significant amount of C buildup was observed at lower binding energies of ∼284.5 eV corresponding to adventitious C and hydrocarbon contamination with a small shoulder at ∼288.7 eV corresponding to the carboxylate functionality (Figure 3g). This data therefore demonstrates that Li_2CO_3 does not form on BN/LLZT even after 2 months of ambient exposure.

The XPS of the B 1s feature in Figure S7a (Supporting Information) shows a small increase in intensity with increasing exposure times. This suggests some oxidation or hydroxylation of boron in BN or BN_xO_y layers. However, the B 1s spectrum in the inset shows the presence of boron even after 2 months of air exposure, indicating that boron remains intact on the surface and is not lost in the form of volatile boric acid. Figure S7b (Supporting Information) shows a significant decrease in the N 1s intensity and a slight shift in binding energy from 398.7 to 398.4 eV, with increasing exposure times. The loss in N 1s intensity at higher binding energies may indicate some desorption of N in the form of volatile NH_x or NO_x species.[63] Similar nitrogen loss is observed upon the exposure of BN/B_2O_3/Si to air[55] and h-BN/Ir films to atomic oxygen at room temperature.[64] N−H bonds arise from unreacted NH_3 and are necessary for the edge termination of BN.[65] Another study showed that BN films deposited using the NH_3 precursor result in some H incorporation into the growing BN film.[66] The Li 1s spectrum in Figure S7c (Supporting Information) demonstrates only a slight attenuation after 2 h in air and a subsequent increase in intensity during 2 months of storage. Figures S7c and S8 (Supporting Information) also show no shift in the binding energy of Li 1s that would suggest lithium hydroxide or lithium carbonate formation.

The results shown in Figure 3g,f and Figures S7a−c and S8 (Supporting Information) demonstrate that although the N sites in the h-BN/BN_xO_y cap are affected during ambient exposures, no lithium carbonate is formed even after 2 months of storage in air. These results demonstrate that ∼3 nm of h-BN/BN_xO_y coating efficiently protected the LLZT surface from atmospheric moisture and prevented Li_2CO_3 and LiOH formation. In addition, such N vacancies could be beneficial to Li-ion transport since (electrochemical) conduction in SSEs occurs through vacancies and defect sites. Recent studies also

https://doi.org/10.1021/acs.chemmater.1c00747
Chem. Mater. 2021, 33, 3401−3412

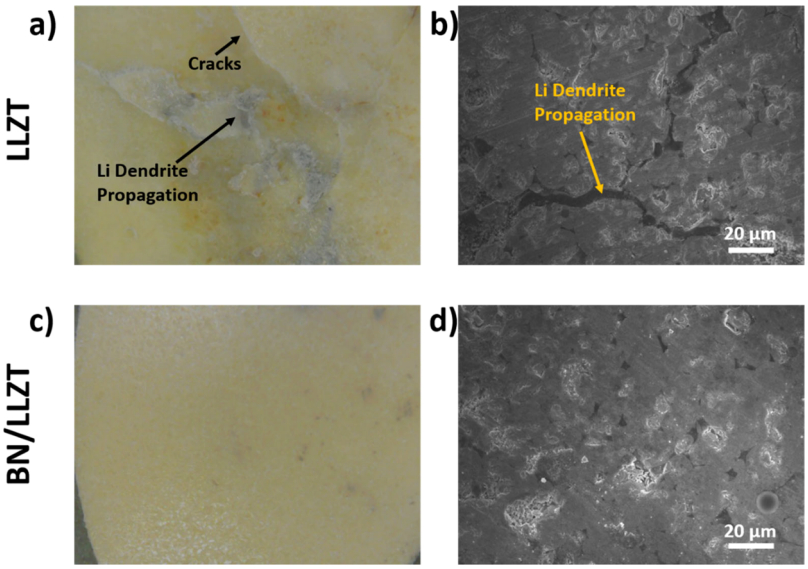

Figure 5. (a,c) Optical microscopy images obtained using a 30× lens and (b,d) FE-SEM images of (a,b) as-synthesized LLZT and (c,d) h-BN-coated LLZT.

show that nitrogen in BN can be restored by heating in a N_2 atmosphere at >427 °C.[67] The effective passivation of the LLZT electrolyte from moisture-induced degradation can be attributed to the superior chemical inertness and hydrophobic property of h-BN as demonstrated in our previous study using exfoliated h-BN nanosheets.[35] In the case of the h-BN nanosheets, moisture could penetrate through the grain boundaries to reach the LLZT surface, resulting in a slight increase in the carbonate level. However, as in our case, h-BN deposited through growth techniques directly on LLZT presents no such grain boundaries and effectively passivates the surface from further degradation.

Surface Wetting Properties and Li Plating/Stripping Studies Using Symmetrical Cells. Thin Li foil was placed on the pellet above where 6 stainless steel spacers were placed and heated at 220 °C for 1 h to study the wettability of pellets with metallic lithium. For as-synthesized LLZT, as shown in Figure 4a, only a small area of Li is in contact with the LLZT pellet, demonstrating poor wetting characteristics with Li. A large gap of about 1−3 μm separates Li and LLZT that may lead to very high polarization and interfacial resistance. In contrast, BN/LLZT demonstrated very high adhesion to metallic Li. No presence of voids and gaps could be observed in the FE-SEM image, proving the high wettability of such surfaces with Li. This high adhesion is due to the synergistic effect of the sputtering process, which produces ultraclean LLZT surfaces, free of Li_2CO_3 and LiOH that are lithophobic in nature. Ultrathin (~3 nm) BN also improves the wettability of Li through weak Lewis acid−base interactions.[68]

Li|LLZT|Li symmetrical cells were made and transferred to a custom-made Swagelok cell that can apply a pressure of 126 kPa. The critical current density (CCD) is the lowest current density at which the shortening of the symmetrical cell occurs due to the propagation of the Li metal across the SSE. CCD for dendrite propagation through the BN/LLZT cell was found to be 0.9 mA cm^{-2} (Figure 4b). In contrast, the CCD for as-synthesized LLZT is 0.25 mA cm^{-2} at 60 °C, as reported in our previous study.[35] The value of the CCD obtained for the BN/LLZT cell is higher than what is reported previously by using surface chemistry or interlayer-based approaches.[21,35,69]

Interfacial resistance was evaluated using electrochemical impedance spectroscopy (EIS) measurements of the symmetrical cell at 60 °C, as shown in Figure 4c. The obtained EIS plot was curve-fitted using the equivalent circuit, "$R_1 + R_2/Q_2 + R_3/Q_3 + R_4/Q_4$", as shown in Figure S9 (Supporting Information), where R_1, R_2, R_3, and R_4 are the solution resistance, bulk resistance, grain boundary resistance, and interfacial resistance, respectively. As two identical interfaces are involved, R_4 was divided by two to get the actual interfacial resistance. An ultralow interfacial resistance of 18 Ω cm^2 was achieved at 60 °C for the BN/LLZT cell, owing to the highly uniform contact of metallic Li with LLZT. On the other hand, the EIS of the as-synthesized LLZT cell cannot be distinguished into individual components, and the values of bulk and grain boundary resistances were obtained from the EIS of BN/LLZT cell. The simulation results showed a very large interfacial resistance of 1145 Ω cm^2 resulting from poor interfacial contact between Li and LLZT. Interfacial resistance obtained from BN/LLZT is indeed one of the lowest values achieved to date. Although Han et al. reported an interfacial resistance of 1 Ω cm^2 for Al_2O_3-coated $Li_7La_{2.75}Ca_{0.25}Zr_{1.75}Nb_{0.25}O_{12}$, the measurement was made by extrapolating d.c. cycling results and not measured directly using EIS.[24] Further, Al_2O_3 forms a Li−Al alloy that may not prevent the electron tunneling across the interface, which has been proven to be the reason for the propagation of Li dendrites.[14]

Direct current (d.c.) Li plating/stripping experiments (30 min plating/stripping) were carried out at different current densities at 60 °C to characterize Li-ion transport across the interface. At a 0.2 mA cm^{-2} current density, the BN/LLZT symmetrical cell initially exhibited very low overpotentials of 10 to 12 mV after 400 h of operation (Figure S10, Supporting Information). At a higher current density of 0.5 mA cm^{-2}, the symmetrical cell exhibited stable cycling for over 200 h with a constant polarization of 27 mV, as seen in Figure 4d. Such low polarization is only possible with well-adhered interfaces that offer negligible interfacial resistance. Further, the possible mechanism of Li-ion conduction is through the defect sites of the deposited layer, such as dangling bonds of boron and

https://doi.org/10.1021/acs.chemmater.1c00747
Chem. Mater. 2021, 33, 3401−3412

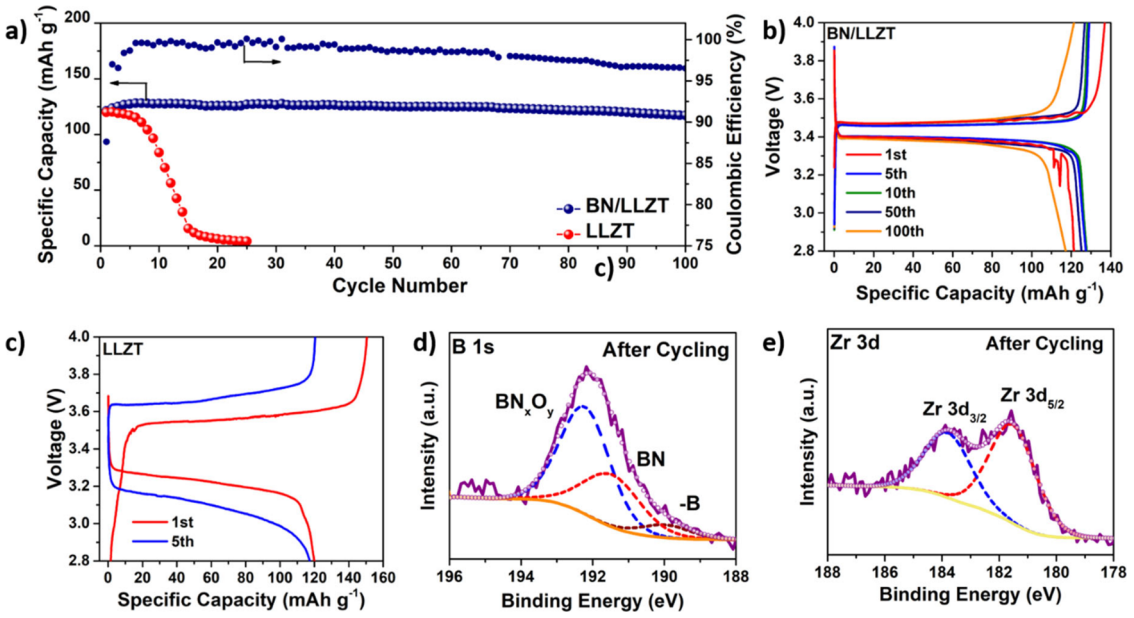

Figure 6. (a) Galvanostatic charge/discharge of all-solid-state batteries. Charge−discharge voltage profile of the ASSB made using (b) BN/LLZT and (c) as-synthesized LLZT. XPS of (d) B 1s and (e) Zr 3d performed on the surface of the BN/LLZT pellet after 103 charge/discharge cycles.

vacancy sites of nitrogen present in the h-BN layer as characterized and discussed earlier. As-synthesized LLZT exhibited a noisy signal with large polarization at a lower current density of 0.2 mA cm^{-2} (Figure S11, Supporting Information), which is due to the nonuniform interfacial contact between LLZT and Li.

Postmortem analysis after Li plating/stripping was carried out on both as-synthesized and h-BN-coated surface-cleaned LLZT pellets using optical microscopy and FE-SEM. As seen on Figure 5a, the penetration of the Li metal is evident through spots marked in the figure even at a lower current density of 0.2 mA cm^{-2}. Further, the propagation of the Li metal induced cracks on the surface. The Li metal was also observed to propagate through these cracks, as seen in the FE-SEM image (Figure 5b). The nonuniform contact between LLZT and Li results in increased Li-ion flux in the regions that are in contact with the Li metal, which further creates high stress resulting in the formation of cracks. In contrast, BN/LLZT did not show any such deposits of metallic Li or crack formation even after cycling for 200 h at 0.5 mA cm^{-2} (Figure 5c,d), which also proves the existence of a homogeneous Li-ion flux. The data from stable Li plating/stripping demonstrates the inhibition of Li dendrite propagation across the interface in BN/LLZT pellets. These observations are consistent with (i) good adherence at the interface, (ii) the absence of surface impurities that induce Li dendrite propagation, (iii) ultrathin h-BN coating that prevents electron tunneling across the interface, (iv) creation of a uniform Li-ion flux across the interface, and (v) excellent mechanical and chemical properties of h-BN.

Full-Cell Performance. All-solid-state batteries (ASSBs) were assembled using $LiFePO_4$ (LFP), LLZT, and Li as the cathode, the electrolyte, and the anode, respectively. The ASSBs were cycled at a C/5 rate at 60 °C, as shown in Figure 6, to evaluate the electrochemical and mechanical stability of the interface with cycling. The LFP cathode was preferred due to its more stable chemistry than other conventional cathodes at elevated temperatures. The ASSB was fabricated using as-synthesized LLZT, which showed drastic capacity loss right after a few cycles, which can be attributed to the loss in contact due to the volume expansion and contraction during the charge/discharge process (Figure 6a). The ASSB made using BN/LLZT exhibited a stable capacity of 130 mAh g^{-1} for over 100 cycles after a few initial cycles of activation. The ASSB delivered a capacity of 119 mAh g^{-1} on the 100th cycle, i.e., a negligible capacity fade of 0.11 mAh g^{-1} per cycle, and the average Coulombic efficiency was calculated to be 98.4%. The voltage profile was found to be long and flat, indicating the fast Li-ion transport across the solid−solid interface. Also, the BN/LLZT cell exhibited a very small increase in polarization with cycling, 57 and 82 mV at the 2nd and 50th cycles, respectively, at a charge/discharge rate of C/5. Small spikes observed in the first cycle are due to temperature fluctuations of the oven while opening and closing. On the other hand, the voltage profile of the as-synthesized LLZT cell showed a very large polarization of 310 mV in the first cycle due to the nonadherent interface formed, and this further increased to 550 mV at the fifth cycle. The voltage plateau was also not flat indicating the increasing impedance to the flow of Li ions across the interface during cycling. Further, the Coulombic efficiency dropped below 50% within the first few cycles (Supporting Information, Figure S12). Figure S13 (Supporting Information) shows the rate capability performance of the ASSB with BN/LLZT at different current densities, from 50 to 500 μA cm^{-2}. The ASSB exhibited a discharge capacity of 146 mAh g^{-1} at 50 μA cm^{-2}, 138 mAh g^{-1} at 100 μA cm^{-2}, 124 mAh g^{-1} at 300 μA cm^{-2}, and 99 mAh g^{-1} at 500 μA cm^{-2} (~1 C rate approx.). The capacity changed back to 138 mAh g^{-1} when the current was changed to 50 μA cm^{-2}, revealing the excellent rate performance of the BN/LLZT cell. After cycling, the Li metal anode was scraped out of the ASSB inside a glovebox, and the LLZT pellet was analyzed using XPS. The B 1s spectrum in Figure 6d indicates the presence of B_N, BN_xO_y, and dangling B bonds, similar to the as-deposited h-BN XPS shown in Figure 2d, without any significant peak shifts. This demonstrates that conformal h-BN coating is chemically stable and that the

https://doi.org/10.1021/acs.chemmater.1c00747
Chem. Mater. 2021, 33, 3401−3412

presence of the defect sites (dangling B bonds) after cycling proves the extent of chemical inertness of h-BN during battery cycling measurements. An increase in the BN_xO_y peak is observed as few layers of h-BN capping the BN_xO_y layer might have been removed while scraping out the lithium metal anode. The well-resolved Zr 3d spectrum in Figure 6b indicates the absence of surface contamination after cycling, which would not have been visible if surface impurities were present.[22]

CONCLUSIONS

Here, we report an effective strategy of combining surface chemistry and interlayer-based mechanisms to tailor the interface between Li and garnet-type SSEs. Pristine LLZT pellets without Li_2CO_3 contamination were obtained by either argon-ion sputtering at 27−227 °C or UHV annealing at 777 °C. Air exposures of pristine LLZT revealed spontaneous Li_2CO_3 formation in less than 10 min. Approximately 3.6 nm of combined h-BN and BN_xO_y film was deposited on both sides using ALD, immediately after surface cleaning using either cleaning approaches, which passivated and protected the LLZT pellets for over 2 months of air exposure. h-BN/BN_xO_y-coated LLZT (BN/LLZT) also demonstrated an ultralow interfacial resistance of 18 Ω cm^2 at 60 °C and yielded a high critical current density of 0.9 mA cm^{-2}. Stable, dendrite-free Li plating/stripping has also been recorded for Li|BN/LLZT|Li symmetrical cells for over 200 cycles at 0.5 mA cm^{-2}. Furthermore, a stable full-cell capacity of 130 mAh g^{-1} was observed for $LiFePO_4$|BN/LLZT|Li cell configuration for over 100 cycles with an average Coulombic efficiency of 98.4%. This study therefore clarifies that inclusion of an interlayer is always required to prevent degradation of garnet-type SSEs in ambient storage and transfers, and the interlayer must be modified to prevent electron tunneling across the electrolyte that induces lithium dendrites.

ASSOCIATED CONTENT

Supporting Information

The Supporting Information is available free of charge at https://pubs.acs.org/doi/10.1021/acs.chemmater.1c00747.

Characterization of the as-synthesized LLZT samples, HAADF-STEM mapping of elements during atmospheric exposure, XP spectra of B 1s, N 1s, and Li 1s during atmospheric exposure of LLZT and BN/LLZT, EIS curve fitting, and rate capability measurements (PDF)

AUTHOR INFORMATION

Corresponding Authors

Jeffry Kelber − *Department of Chemistry, University of North Texas, Denton, Texas 76203-1277, United States*; Email: kelber@unt.edu

Leela Mohana Reddy Arava − *Department of Mechanical Engineering, Wayne State University, Detroit, Michigan 48201, United States*; orcid.org/0000-0001-6685-6061; Email: leela.arava@wayne.edu

Authors

Sathish Rajendran − *Department of Mechanical Engineering, Wayne State University, Detroit, Michigan 48201, United States*

Aparna Pilli − *Department of Chemistry, University of North Texas, Denton, Texas 76203-1277, United States*

Olatomide Omolere − *Department of Chemistry, University of North Texas, Denton, Texas 76203-1277, United States*

Complete contact information is available at: https://pubs.acs.org/10.1021/acs.chemmater.1c00747

Author Contributions

[§]S.R. and A.P. contributed equally.

Notes

The authors declare no competing financial interest.

ACKNOWLEDGMENTS

This work was supported in part by the National Science Foundation under grant no. 1751472. The authors thank the Lumigen Instrument Centre at Wayne State University for the use of FE-SEM (NSF: MRI 0922912) and XPS (NSF: MRI 1849578) facilities. A.P., O.O., and J.K. would like to acknowledge the contributions of J. Jones and N. Chugh.

REFERENCES

(1) Lin, D.; Liu, Y.; Cui, Y. Reviving the lithium metal anode for high-energy batteries. *Nat. Nanotechnol.* **2017**, *12*, 194−206.

(2) Armand, M.; Tarascon, J. M. Building better batteries. *Nature* **2008**, *451*, 652−657.

(3) Tarascon, J.-M.; Armand, M. Issues and challenges facing rechargeable lithium batteries. In *Materials for sustainable energy: a collection of peer-reviewed research and review articles from Nature Publishing Group*; World Scientific: 2011; pp. 171−179.

(4) Cheng, X. B.; Zhang, R.; Zhao, C. Z.; Zhang, Q. Toward Safe Lithium Metal Anode in Rechargeable Batteries: A Review. *Chem. Rev.* **2017**, *117*, 10403−10473.

(5) Manthiram, A.; Yu, X.; Wang, S. Lithium battery chemistries enabled by solid-state electrolytes. *Nat. Rev. Mater.* **2017**, *2*, 16103−16116.

(6) Bachman, J. C.; Muy, S.; Grimaud, A.; Chang, H. H.; Pour, N.; Lux, S. F.; Paschos, O.; Maglia, F.; Lupart, S.; Lamp, P.; Giordano, L.; Shao-Horn, Y. Inorganic Solid-State Electrolytes for Lithium Batteries: Mechanisms and Properties Governing Ion Conduction. *Chem. Rev.* **2016**, *116*, 140−162.

(7) Liu, Q.; Geng, Z.; Han, C.; Fu, Y.; Li, S.; He, Y.-b.; Kang, F.; Li, B. Challenges and perspectives of garnet solid electrolytes for all solid-state lithium batteries. *J. Power Sources* **2018**, *389*, 120−134.

(8) Jones, J. C.; Rajendran, S.; Pilli, A.; Lee, V.; Chugh, N.; Arava, L. M. R.; Kelber, J. A. In situ x-ray photoelectron spectroscopy study of lithium carbonate removal from garnet-type solid-state electrolyte using ultra high vacuum techniques. *J. Vac. Sci. Technol., A* **2020**, *38*, No. 023201.

(9) Ma, C.; Cheng, Y.; Yin, K.; Luo, J.; Sharafi, A.; Sakamoto, J.; Li, J.; More, K. L.; Dudney, N. J.; Chi, M. Interfacial Stability of Li Metal-Solid Electrolyte Elucidated via in Situ Electron Microscopy. *Nano Lett.* **2016**, *16*, 7030−7036.

(10) Rettenwander, D.; Wagner, R.; Reyer, A.; Bonta, M.; Cheng, L.; Doeff, M. M.; Limbeck, A.; Wilkening, M.; Amthauer, G. Interface Instability of Fe-Stabilized $Li_7La_3Zr_2O_{12}$ versus Li Metal. *J. Phys. Chem. C* **2018**, *122*, 3780−3785.

(11) Zhang, W.; Richter, F. H.; Culver, S. P.; Leichtweiss, T.; Lozano, J. G.; Dietrich, C.; Bruce, P. G.; Zeier, W. G.; Janek, J. Degradation Mechanisms at the $Li_{10}GeP_2S_{12}/LiCoO_2$ Cathode Interface in an All-Solid-State Lithium-Ion Battery. *ACS Appl. Mater. Interfaces* **2018**, *10*, 22226−22236.

(12) Brugge, R. H.; Hekselman, A. K. O.; Cavallaro, A.; Pesci, F. M.; Chater, R. J.; Kilner, J. A.; Aguadero, A. Garnet Electrolytes for Solid State Batteries: Visualization of Moisture-Induced Chemical Degradation and Revealing Its Impact on the Li-Ion Dynamics. *Chem. Mater.* **2018**, *30*, 3704−3713.

(13) Galven, C.; Fourquet, J.-L.; Crosnier-Lopez, M.-P.; Le Berre, F. Instability of the Lithium Garnet $Li_7La_3Sn_2O_{12}$: Li^+/H^+ Exchange and Structural Study. *Chem. Mater.* **2011**, *23*, 1892−1900.
(14) Han, F.; Westover, A. S.; Yue, J.; Fan, X.; Wang, F.; Chi, M.; Leonard, D. N.; Dudney, N. J.; Wang, H.; Wang, C. High electronic conductivity as the origin of lithium dendrite formation within solid electrolytes. *Nat. Energy* **2019**, *4*, 187−196.
(15) Nagao, M.; Hayashi, A.; Tatsumisago, M. High-capacity Li 2 S−nanocarbon composite electrode for all-solid-state rechargeable lithium batteries. *J. Mater. Chem.* **2012**, *22*, 10015−10020.
(16) Ito, S.; Fujiki, S.; Yamada, T.; Aihara, Y.; Park, Y.; Kim, T. Y.; Baek, S. W.; Lee, J. M.; Doo, S.; Machida, N. A rocking chair type all-solid-state lithium ion battery adopting Li_2O-ZrO_2 coated $LiNi_{0.8}Co_{0.15}Al_{0.05}O_2$ and a sulfide based electrolyte. *J. Power Sources* **2014**, *248*, 943−950.
(17) Chen, L.; Li, Y.; Li, S.-P.; Fan, L.-Z.; Nan, C.-W.; Goodenough, J. B. PEO/garnet composite electrolytes for solid-state lithium batteries: From "ceramic-in-polymer" to "polymer-in-ceramic". *Nano Energy* **2018**, *46*, 176−184.
(18) Cheng, S. H. S.; He, K. Q.; Liu, Y.; Zha, J. W.; Kamruzzaman, M.; Ma, R. L. W.; Dang, Z. M.; Li, R. K. Y.; Chung, C. Y. Electrochemical performance of all-solid-state lithium batteries using inorganic lithium garnets particulate reinforced PEO/$LiClO_4$ electrolyte. *Electrochim. Acta* **2017**, *253*, 430−438.
(19) Wang, J. Z.; Zhong, C.; Wexler, D.; Idris, N. H.; Wang, Z. X.; Chen, L. Q.; Liu, H. K. Graphene-encapsulated Fe_3O_4 nanoparticles with 3D laminated structure as superior anode in lithium ion batteries. *Chem. Eur. J.* **2011**, *17*, 661−667.
(20) Baggetto, L.; Niessen, R. A. H.; Roozeboom, F.; Notten, P. H. L. High energy density all-solid-state batteries: a challenging concept towards 3D integration. *Adv. Funct. Mater.* **2008**, *18*, 1057−1066.
(21) Sharafi, A.; Kazyak, E.; Davis, A. L.; Yu, S.; Thompson, T.; Siegel, D. J.; Dasgupta, N. P.; Sakamoto, J. Surface Chemistry Mechanism of Ultra-Low Interfacial Resistance in the Solid-State Electrolyte $Li_7La_3Zr_2O_{12}$. *Chem. Mater.* **2017**, *29*, 7961−7968.
(22) Li, Y.; Chen, X.; Dolocan, A.; Cui, Z.; Xin, S.; Xue, L.; Xu, H.; Park, K.; Goodenough, J. B. Garnet Electrolyte with an Ultralow Interfacial Resistance for Li-Metal Batteries. *J. Am. Chem. Soc.* **2018**, *140*, 6448−6455.
(23) Wang, C.; Gong, Y.; Liu, B.; Fu, K.; Yao, Y.; Hitz, E.; Li, Y.; Dai, J.; Xu, S.; Luo, W.; Wachsman, E. D.; Hu, L. Conformal, Nanoscale ZnO Surface Modification of Garnet-Based Solid-State Electrolyte for Lithium Metal Anodes. *Nano Lett.* **2017**, *17*, 565−571.
(24) Han, X.; Gong, Y.; Fu, K. K.; He, X.; Hitz, G. T.; Dai, J.; Pearse, A.; Liu, B.; Wang, H.; Rubloff, G.; Mo, Y.; Thangadurai, V.; Wachsman, E. D.; Hu, L. Negating interfacial impedance in garnet-based solid-state Li metal batteries. *Nat. Mater.* **2017**, *16*, 572−579.
(25) Yan, K.; Lee, H. W.; Gao, T.; Zheng, G.; Yao, H.; Wang, H.; Lu, Z.; Zhou, Y.; Liang, Z.; Liu, Z.; Chu, S.; Cui, Y. Ultrathin two-dimensional atomic crystals as stable interfacial layer for improvement of lithium metal anode. *Nano Lett.* **2014**, *14*, 6016−6022.
(26) Xu, H.; Li, Y.; Zhou, A.; Wu, N.; Xin, S.; Li, Z.; Goodenough, J. B. Li_3N-Modified Garnet Electrolyte for All-Solid-State Lithium Metal Batteries Operated at 40 °C. *Nano Lett.* **2018**, *18*, 7414−7418.
(27) Puurunen, R. L. Surface chemistry of atomic layer deposition: A case study for the trimethylaluminum/water process. *J. Appl. Phys.* **2005**, *97*, 121301.
(28) George, S. M. Atomic layer deposition: an overview. *Chem. Rev.* **2010**, *110*, 111−131.
(29) Woo, J. H.; Trevey, J. E.; Cavanagh, A. S.; Choi, Y. S.; Kim, S. C.; George, S. M.; Oh, K. H.; Lee, S.-H. Nanoscale interface modification of $LiCoO_2$ by Al_2O_3 atomic layer deposition for solid-state Li batteries. *J. Electrochem. Soc.* **2012**, *159*, A1120−A1124.
(30) Liu, Y.; Sun, Q.; Zhao, Y.; Wang, B.; Kaghazchi, P.; Adair, K. R.; Li, R.; Zhang, C.; Liu, J.; Kuo, L.-Y.; Hu, Y.; Sham, T.-K.; Zhang, L.; Yang, R.; Lu, S.; Song, X.; Sun, X. Stabilizing the interface of NASICON solid electrolyte against Li metal with atomic layer deposition. *ACS Appl. Mater. Interfaces* **2018**, *10*, 31240−31248.
(31) Song, L.; Ci, L.; Lu, H.; Sorokin, P. B.; Jin, C.; Ni, J.; Kvashnin, A. G.; Kvashnin, D. G.; Lou, J.; Yakobson, B. I.; Ajayan, P. M. Large scale growth and characterization of atomic hexagonal boron nitride layers. *Nano Lett.* **2010**, *10*, 3209−3215.
(32) Golberg, D.; Bando, Y.; Huang, Y.; Terao, T.; Mitome, M.; Tang, C.; Zhi, C. Boron nitride nanotubes and nanosheets. *ACS Nano* **2010**, *4*, 2979−2993.
(33) Weber, M.; Coy, E.; Iatsunskyi, I.; Yate, L.; Miele, P.; Bechelany, M. Mechanical properties of boron nitride thin films prepared by atomic layer deposition. *CrystEngComm* **2017**, *19*, 6089−6094.
(34) Falin, A.; Cai, Q.; Santos, E. J. G.; Scullion, D.; Qian, D.; Zhang, R.; Yang, Z.; Huang, S.; Watanabe, K.; Taniguchi, T.; Barnett, M. R.; Chen, Y.; Ruoff, R. S.; Li, L. H. Mechanical properties of atomically thin boron nitride and the role of interlayer interactions. *Nat. Commun.* **2017**, *8*, 15815.
(35) Rajendran, S.; Thangavel, N. K.; Mahankali, K.; Arava, L. M. R. Toward Moisture-Stable and Dendrite-Free Garnet-Type Solid-State Electrolytes. *ACS Appl. Energy Mater.* **2020**, *3*, 6775−6784.
(36) Pilli, A.; Jones, J.; Lee, V.; Chugh, N.; Kelber, J.; Pasquale, F.; LaVoie, A. In situ XPS study of low temperature atomic layer deposition of B_2O_3 films on Si using BCl3 and H2O precursors. *J. Vac. Sci. Technol., A* **2018**, *36*, No. 061503.
(37) Kalkofen, B.; Amusan, A. A.; Bukhari, M. S. K.; Garke, B.; Lisker, M.; Gargouri, H.; Burte, E. P. Use of B_2O_3 films grown by plasma-assisted atomic layer deposition for shallow boron doping in silicon. *J. Vac. Sci. Technol., A* **2015**, *33*, No. 031512.
(38) Wang, M. J.; Carmona, E.; Gupta, A.; Albertus, P.; Sakamoto, J. Enabling "lithium-free" manufacturing of pure lithium metal solid-state batteries through in situ plating. *Nat. Commun.* **2020**, *11*, 5201−5209.
(39) Yan, X.; Li, Z.; Wen, Z.; Han, W. Li/$Li_7La_3Zr_2O_{12}$/$LiFePO_4$ All-Solid-State Battery with Ultrathin Nanoscale Solid Electrolyte. *J. Phys. Chem. C* **2017**, *121*, 1431−1435.
(40) Sunding, M. F.; Hadidi, K.; Diplas, S.; Løvvik, O. M.; Norby, T. E.; Gunnæs, A. E. XPS characterisation of in situ treated lanthanum oxide and hydroxide using tailored charge referencing and peak fitting procedures. *J. Electron Spectrosc. Relat. Phenom* **2011**, *184*, 399−409.
(41) Tanuma, S.; Powell, C. J.; Penn, D. R. Calculation of electron inelastic mean free paths (IMFPs) VII. Reliability of the TPP-2M IMFP predictive equation. *Surf. Interface Anal.* **2003**, *35*, 268−275.
(42) Kataoka, K.; Akimoto, J. High Ionic Conductor Member of Garnet-Type Oxide $Li_{6.5}La_3Zr_{1.5}Ta_{0.5}O_{12}$. *ChemElectroChem* **2018**, *5*, 2551−2557.
(43) Kataoka, K.; Akimoto, J. Lithium-ion conductivity and crystal structure of garnet-type solid electrolyte $Li_{7-x}La_3Zr_{2-x}Ta_xO_{12}$ using single-crystal. *J. Ceram. Soc. Japan* **2019**, *127*, 521−526.
(44) Badami, P.; Weller, J. M.; Wahab, A.; Redhammer, G.; Ladenstein, L.; Rettenwander, D.; Wilkening, M.; Chan, C. K.; Kannan, A. N. M. Highly Conductive Garnet-Type Electrolytes: Access to $Li_{6.5}La_3Zr_{1.5}Ta_{0.5}O_{12}$ Prepared by Molten Salt and Solid-State Methods. *ACS Appl. Mater. Interfaces* **2020**, *12*, 48580−48590.
(45) Fu, K. K.; Gong, Y. H.; Liu, B. Y.; Zhu, Y. Z.; Xu, S. M.; Yao, Y. G.; Luo, W.; Wang, C. W.; Lacey, S. D.; Dai, J. Q.; Chen, Y. N.; Mo, Y. F.; Wachsman, E.; Hu, L. B. Toward garnet electrolyte-based Li metal batteries: An ultrathin, highly effective, artificial solid-state electrolyte/metallic Li interface. *Sci. Adv.* **2017**, *3*, No. e1601659.
(46) Herstedt, M.; Abraham, D. P.; Kerr, J. B.; Edström, K. X-ray photoelectron spectroscopy of negative electrodes from high-power lithium-ion cells showing various levels of power fade. *Electrochim. Acta* **2004**, *49*, 5097−5110.
(47) Onwumere, J.; Piątek, J.; Budnyak, T.; Chen, J.; Budnyk, S.; Karim, Z.; Thersleff, T.; Kuśtrowski, P.; Mathew, A. P.; Slabon, A. CelluPhot: Hybrid Cellulose-Bismuth Oxybromide Membrane for Pollutant Removal. *ACS Appl. Mater. Interfaces* **2020**, *12*, 42891−42901.
(48) Zhang, Y.; Savara, A.; Mullins, D. R. Ambient-Pressure XPS Studies of Reactions of Alcohols on $SrTiO_3$(100). *J. Phys. Chem. C* **2017**, *121*, 23436−23445.

(49) Cheng, L.; Liu, M.; Mehta, A.; Xin, H.; Lin, F.; Persson, K.; Chen, G.; Crumlin, E. J.; Doeff, M. Garnet Electrolyte Surface Degradation and Recovery. *ACS Appl. Energy Mater.* **2018**, *1*, 7244.
(50) Kanamura, K.; Tamura, H.; Shiraishi, S.; Takehara, Z.-I. XPS analysis for the lithium surface immersed in γ-butyrolactone containing various salts. *Electrochim. Acta* **1995**, *40*, 913−921.
(51) An, S. J.; Li, J.; Sheng, Y.; Daniel, C.; Wood, D. L., III Long-Term Lithium-Ion Battery Performance Improvement via Ultraviolet Light Treatment of the Graphite Anode. *J. Electrochem. Soc.* **2016**, *163*, A2866−A2875.
(52) Qu, J.; Li, Q.; Luo, C.; Cheng, J.; Hou, X. Characterization of Flake Boron Nitride Prepared from the Low Temperature Combustion Synthesized Precursor and Its Application for Dye Adsorption. *Coatings* **2018**, *8*, 214.
(53) Firestein, K. L.; Leybo, D. V.; Steinman, A. E.; Kovalskii, A. M.; Matveev, A. T.; Manakhov, A. M.; Sukhorukova, I. V.; Slukin, P. V.; Fursova, N. K.; Ignatov, S. G.; Golberg, D. V.; Shtansky, D. V. BN/Ag hybrid nanomaterials with petal-like surfaces as catalysts and antibacterial agents. *Beilstein J. Nanotechnol.* **2018**, *9*, 250−261.
(54) Cheng, Q.; Li, A.; Li, N.; Li, S.; Zangiabadi, A.; Li, T.-D.; Huang, W.; Li, A. C.; Jin, T.; Song, Q.; Xu, W.; Ni, N.; Zhai, H.; Dontigny, M.; Zaghib, K.; Chuan, X.; Su, D.; Yan, K.; Yang, Y. Stabilizing Solid Electrolyte-Anode Interface in Li-Metal Batteries by Boron Nitride-Based Nanocomposite Coating. *Joule* **2019**, *3*, 1510−1522.
(55) Pilli, A.; Jones, J.; Chugh, N.; Kelber, J.; Pasquale, F.; LaVoie, A. Atomic layer deposition of BN as a novel capping barrier for B_2O_3. *J. Vac. Sci. Technol., A* **2019**, *37*, No. 041505.
(56) Sugino, T.; Tagawa, S. Effect of oxygen plasma treatment on field emission characteristics of boron-nitride films. *Appl. Phys. Lett.* **1999**, *74*, 889−891.
(57) Guimon, C.; Gonbeau, D.; G. P ster-Guillouzo, O.; Dugne, A.; Guette, R.; Naslain, M.; Lahaye, M. XPS study of BN thin films deposited by CVD on SiC plane substrates. *Surf. Interface Anal.* **1990**, *16*, 440.
(58) Huo, H.; Liang, J.; Zhao, N.; Li, X.; Lin, X.; Zhao, Y.; Adair, K.; Li, R.; Guo, X.; Sun, X. Dynamics of the Garnet/Li Interface for Dendrite-Free Solid-State Batteries. *ACS Energy Lett.* **2020**, *5*, 2156−2164.
(59) Wood, K. N.; Teeter, G. XPS on Li-Battery-Related Compounds: Analysis of Inorganic SEI Phases and a Methodology for Charge Correction. *ACS Appl. Energy Mater.* **2018**, *1*, 4493−4504.
(60) Oswald, S.; Thoss, F.; Zier, M.; Hoffmann, M.; Jaumann, T.; Herklotz, M.; Nikolowski, K.; Scheiba, F.; Kohl, M.; Giebeler, L.; Mikhailova, D.; Ehrenberg, H. Binding Energy Referencing for XPS in Alkali Metal-Based Battery Materials Research (II): Application to Complex Composite Electrodes. *Batteries* **2018**, *4*, 36.
(61) Zhang, T.; Christopher, T. D.; Huang, S.; Liu, Y.'g.; Gao, W.; Söhnel, T.; Cao, P. Pressureless sintering of Al-free Ta-doped lithium garnets $Li_{7-x}La3Zr_{2-x}Ta_xO12$ and the degradation mechanism in humid air. *Ceram. Int.* **2019**, *45*, 20954−20960.
(62) Truong, L.; Thangadurai, V. Soft-Chemistry of Garnet-Type $Li_{5+x}Ba_xLa_{3-x}Nb_2O_{12}$ (x= 0, 0.5, 1): Reversible $H^+ \leftrightarrow Li^+$ Ion-Exchange Reaction and Their X-ray, ^{7}Li MAS NMR, IR, and AC Impedance Spectroscopy Characterization. *Chem. Mater.* **2011**, *23*, 3970−3977.
(63) Kobelev, A.; Barsukov, Y. V.; Andrianov, N.; Smirnov, A. Boron trichloride plasma treatment effect on ohmic contact resistance formed on GaN-based epitaxial structure. *Journal of Physics: Conference Series*; IOP Publishing: 2015, p 012013.
(64) Simonov, K. A.; Vinogradov, N. A.; Ng, M. L.; Vinogradov, A. S.; Mårtensson, N.; Preobrajenski, A. B. Controllable oxidation of h-BN monolayer on Ir(111) studied by core-level spectroscopies. *Surf. Sci.* **2012**, *606*, 564−570.
(65) Pakdel, A.; Bando, Y.; Golberg, D. Plasma-assisted interface engineering of boron nitride nanostructure films. *ACS Nano* **2014**, *8*, 10631−10639.
(66) Ferguson, J. D.; Weimer, A. W.; George, S. M. Atomic layer deposition of boron nitride using sequential exposures of BCl_3 and NH_3. *Thin Solid Films* **2002**, *413*, 16−25.
(67) Kidambi, P. R.; Blume, R.; Kling, J.; Wagner, J. B.; Baehtz, C.; Weatherup, R. S.; Schloegl, R.; Bayer, B. C.; Hofmann, S. In Situ Observations during Chemical Vapor Deposition of Hexagonal Boron Nitride on Polycrystalline Copper. *Chem. Mater.* **2014**, *26*, 6380−6392.
(68) Waqas, M.; Ali, S.; Chen, D.; Boateng, B.; Han, Y.; Zhang, M.; Han, J.; Goodenough, J. B.; He, W. A robust bi-layer separator with Lewis acid-base interaction for high-rate capacity lithium-ion batteries. *Composites Part B* **2019**, *177*, 107448.
(69) Tsai, C. L.; Roddatis, V.; Chandran, C. V.; Ma, Q.; Uhlenbruck, S.; Bram, M.; Heitjans, P.; Guillon, O. $Li_7La_3Zr_2O_{12}$ Interface Modification for Li Dendrite Prevention. *ACS Appl. Mater. Interfaces* **2016**, *8*, 10617−10626.

https://doi.org/10.1021/acs.chemmater.1c00747
Chem. Mater. 2021, 33, 3401−3412